# JFM RAPIDS
journals.cambridge.org/rapids

# Subsonic flow past localised heating elements in boundary layers

**A. F. Aljohani**[1,2] **and J. S. B. Gajjar**[2,†]

[1]Department of Mathematics, Faculty of Science, University of Tabuk, Saudi Arabia

[2]School of Mathematics, University of Manchester, Manchester M13 9PL, UK

The problem of subsonic flow past micro-electro-mechanical-system-type (MEMS-type) heating elements placed on a flat surface, where the MEMS devices have hump-shaped surfaces, is investigated using triple-deck theory. The compressible Navier–Stokes equations supplemented by the energy equation are considered in the limit that the Reynolds number is large. The triple-deck problem is formulated, and the linear and nonlinear analysis and results are presented. The current work is a generalisation of the problem discussed by Koroteev & Lipatov (*J. Fluid Mech.*, vol. 707, 2012, pp. 595–605; *Z. Angew. Math. Mech.*, vol. 77, 2013, pp. 486–493), where the MEMS devices have flat-shaped surfaces. The results show that the hump-shaped heating elements enhance large drops in pressure, and peaks and troughs in the skin friction over the centre of the hump compared with the flat-shaped devices, which may be useful for controlling the flow.

**Key words:** aerodynamics, boundary layers, flow control

## 1. Introduction

Flow separation from the surface of a rigid body is one of the most interesting phenomena in fluid motion. This separation causes major effects in flow fields. Investigation of the separation and its consequences is of particular importance in understanding flows at high Reynolds numbers. The explanation of the phenomena of separation lies in the theory of the boundary layer, in particular triple-deck theory, see Neiland (1969), Stewartson & Williams (1969) and Messiter (1970). In recent years, there has been an increasing interest in using micro-electro-mechanical-system (MEMS) devices to control the separation of flow at high Reynolds numbers. Based on triple-deck theory, we investigate subsonic flow past MEMS-type heating elements placed on a flat surface in which the heating element has a humped shape. The current

† Email address for correspondence: jitesh.gajjar@manchester.ac.uk

work reduces to the problem investigated by, for example, Koroteev & Lipatov (2012, 2013) when the MEMS devices have zero hump height. Apart from MEMS devices, another motivation for the current work is to try to understand how local hot spots or cold bumps affect separation.

## 2. Problem formulation

We consider a subsonic viscous flow of a perfect gas past a semi-infinite flat plate on which there is a small heating element. In cross-section, the hump has dimensions that are small compared with those of the oncoming boundary layer along the plate. The Reynolds number $Re = \rho_\infty U_\infty L / \mu_\infty$ is asymptotically large, where $\rho_\infty$, $U_\infty$ and $\mu_\infty$ are the density, the streamwise velocity and the dynamic viscosity coefficient respectively in the undisturbed flow above the surface where the heated section is located, and $L$ is the distance from the leading edge to the energy release domain. Let $Re^{-1/2} = \varepsilon$. We assume that the hump has a length of $O(L\varepsilon^{3/4})$ and a height of $O(L\varepsilon^{5/4})$. In particular, we consider humps that have profiles $y^*/L\varepsilon^{5/4} = \bar{h}F(x^*/L\varepsilon^{3/4})$, where $\bar{h}$ is $O(1)$ and the function $F$ is such that $G(X) = \bar{h}F(X)$ is of order 1. Variables of the governing Navier–Stokes and energy equations are non-dimensionalised, with $U_\infty, L$ and $\rho_\infty$ being the characteristic velocity, length and density scales respectively. Then, we use the following dimensionless variables:

$$\left. \begin{aligned} (x, y) &= \frac{1}{L}(x^*, y^*), \quad (u, v) = \frac{1}{U_\infty}(u^*, v^*), \quad T = \frac{T^*R}{U_\infty^2}, \\ p &= \frac{p^* - p_\infty}{\rho_\infty U_\infty^2}, \quad \mu = \frac{\mu^*}{\mu_\infty} \quad \text{and} \quad \rho = \frac{\rho^*}{\rho_\infty}. \end{aligned} \right\} \tag{2.1}$$

Here, $(x, y)$ are the Cartesian coordinates, $(u, v)$ are the corresponding velocity components, $p$ is the pressure, $T$ is the temperature, $\mu$ is the viscosity, $\rho$ is the density, $R$ is the gas constant and $p_\infty$ is the free-stream pressure. We also introduce the free-stream Mach number $M_\infty = U_\infty/c_\infty$, where $c_\infty = \sqrt{\gamma p_\infty/\rho_\infty}$.

Neiland (1971) has discussed the arguments leading to the triple-deck scales, and Lipatov (2006) and Koroteev & Lipatov (2012, 2013), in particular, have explained how small changes in the surface temperature lead to a nonlinear interaction within the triple deck. The interested reader is referred to these and other papers for more details of the governing equations and expansions. Using this as our starting point, the method of matched asymptotic expansions is used to obtain the equations of the interaction problem. In our case, the main difference between the current and previous work is that we also require no slip on the hump surface. In particular, in the lower deck, the independent variables and expansions are given by

$$\left. \begin{aligned} x &= 1 + \varepsilon^{3/4}X, \quad y = \varepsilon^{5/4}y_3, \\ u &= \varepsilon^{1/4}u_3 + \cdots, \quad v = \varepsilon^{3/4}v_3 + \cdots, \quad p = \varepsilon^{1/2}p_3 + \cdots, \\ \rho &= \rho_3 + \cdots \quad \text{and} \quad T = T_3 + \cdots. \end{aligned} \right\} \tag{2.2}$$

Substitution into the Navier–Stokes equations leads to the lower-deck problem,

$$u_3\frac{\partial \rho_3}{\partial X} + v_3\frac{\partial \rho_3}{\partial y_3} + \rho_3\frac{\partial u_3}{\partial X} + \rho_3\frac{\partial v_3}{\partial y_3} = 0, \tag{2.3}$$

$$\rho_3\left(u_3\frac{\partial u_3}{\partial X} + v_3\frac{\partial u_3}{\partial y_3}\right) = -\frac{\partial p_3}{\partial X} + \frac{\partial}{\partial y_3}\left(\mu\frac{\partial u_3}{\partial y_3}\right), \tag{2.4}$$

$$\frac{\partial p_3}{\partial y_3} = 0, \quad \rho_3 T_3 = 1, \tag{2.5a,b}$$

$$\rho_3 \left( u_3 \frac{\partial T_3}{\partial X} + v_3 \frac{\partial T_3}{\partial y_3} \right) = \frac{\partial}{\partial y_3} \left( \frac{\mu}{Pr} \frac{\partial T_3}{\partial y_3} \right), \tag{2.6}$$

with the boundary and matching conditions

$$\left. \begin{array}{ll} u_3 \to \lambda(y_3 + A(X)), & T_3 \to T_B(x, 0) \quad \text{as } y_3 \to \infty, \\ u_3 = v_3 = 0, & T_3 = T_w(X) \quad \text{on } y_3 = G(X). \end{array} \right\} \tag{2.7}$$

We also have the interaction law

$$p_3(X) = \frac{1}{\pi \sqrt{1 - M_\infty^2}} \int_{-\infty}^{\infty} \frac{\mathcal{A}'(\zeta)}{X - \zeta} \, d\zeta. \tag{2.8}$$

Here, $\mathcal{A}(X)$ is the displacement function, $\lambda = (\partial U_B / \partial y_3)(1, y_3 = 0)$ is the basic shear of the oncoming boundary layer profile $U_B(x, y)$, $T_B(x, y)$ is the basic temperature profile and $G(X)$ is the physical hump shape. As a result, after further employing the Howarth–Dorodnitsyn transformation followed by the Prandtl transformation, using the Chapman viscosity law, setting the Prandtl number to be unity, and scaling to remove some constants, the governing equations and boundary conditions for subsonic flow in the lower deck can be shown to be given by

$$\frac{\partial u_b}{\partial x_b} + \frac{\partial v_b}{\partial y_b} = 0, \tag{2.9}$$

$$u_b \frac{\partial u_b}{\partial x_b} + v_b \frac{\partial u_b}{\partial y_b} + T_b \frac{\partial p_b}{\partial x_b} = \frac{\partial^2 u_b}{\partial y_b^2}, \tag{2.10}$$

$$u_b \frac{\partial T_b}{\partial x_b} + v_b \frac{\partial T_b}{\partial y_b} = \frac{\partial^2 T_b}{\partial y_b^2}, \tag{2.11}$$

$$p_b(x_b) = \frac{1}{\pi} \int_{-\infty}^{\infty} \frac{\mathcal{K}'(s)}{x_b - s} \, ds, \tag{2.12}$$

with the no-slip conditions on $y_b = 0$ given by

$$u_b(x_b, 0) = v_b(x_b, 0) = 0, \tag{2.13}$$

and the prescribed wall temperature

$$T_b(x_b, 0) = T_w(x_b). \tag{2.14}$$

The boundary conditions far from the surface ($y_b \to \infty$) are given by

$$u_b \to y_b + \mathcal{A}(x_b) + H(x_b), \quad \mathcal{K}(x_b) = \mathcal{A}(x_b) + \int_0^\infty (1 - T_b(x_b, \eta)) \, d\eta, \quad T_b(x_b, y_b) \to 1, \tag{2.15a-c}$$

and far upstream

$$\mathcal{A}(-\infty) = 0. \tag{2.16}$$

The interaction condition (2.12) can be represented in another form, as mentioned in Smith (1973), as

$$\mathcal{K}''(x_b) = -\frac{1}{\pi} \int_{-\infty}^{\infty} \frac{p_b'(s)}{x_b - s} \, ds. \tag{2.17}$$

Here, $x_b$ is the scaled streamwise coordinate in the triple deck, $y_b$ is the scaled lower-deck coordinate (following the use of the Dorodnitsyn–Howarth transformation), $u_b(x_b, y_b)$, $v_b(x_b, y_b)$ are the scaled lower-deck velocity components, $T_b(x_b, y_b)$ is the scaled temperature, $p_b(x_b)$ is the induced pressure, $\mathcal{K}(x_b)$ is the total displacement of stream lines, $\mathcal{A}(x_b)$ is the displacement of stream lines caused by the viscosity of the fluid and $T_w(x_b)$ represents the prescribed wall temperature. The function $H(x_b)$ is the shape of the element surface, which is related to the physical hump shape $G(x_b)$ in the original variables by

$$H(x_b) = \int_0^{G(x_b)} \rho_3(x_b, y_b) \, \mathrm{d}y_b. \tag{2.18}$$

The main difference between the present work and that of Koroteev & Lipatov (2012, 2013) is that $H(x_b) = 0$ in the latter.

## 3. Linear theory

In general, to solve (2.9)–(2.17) for variations of the temperature $\Delta T$ of $O(1)$ and $H(x_b)$ of $O(1)$, we require a numerical method. For small variations of the temperature and hump height, we may study the problem analytically in the linear approximation. We consider small variations of the temperature, i.e. $\sigma = \Delta T \ll 1$. We may linearise equations (2.9)–(2.17) related to the undisturbed boundary layer profile by expanding the flow variables as follows:

$$u_b = y_b + \sigma \tilde{U} + O(\sigma^2), \quad v_b = \sigma \tilde{V} + O(\sigma^2), \tag{3.1a,b}$$

$$\mathcal{K} = \sigma \mathcal{K}_1 + O(\sigma^2), \quad T_b = 1 + \sigma \tilde{T} + O(\sigma^2), \tag{3.2a,b}$$

$$p_b = \sigma \tilde{P} + O(\sigma^2), \quad H = \sigma \tilde{H} + O(\sigma^2) \quad \text{and} \quad \mathcal{A} = \sigma \mathcal{A}_1 + O(\sigma^2) \tag{3.3a-c}$$

as $\sigma \to 0$. After substituting the expansions, equations (3.1)–(3.3), into equations and boundary conditions (2.9)–(2.17) we obtain the following linearised problem:

$$\frac{\partial \tilde{U}}{\partial x_b} + \frac{\partial \tilde{V}}{\partial y_b} = 0, \tag{3.4}$$

$$y_b \frac{\partial \tilde{U}}{\partial x_b} + \tilde{V} + \frac{\partial \tilde{P}}{\partial x_b} = \frac{\partial^2 \tilde{U}}{\partial y_b^2}, \tag{3.5}$$

$$y_b \frac{\partial \tilde{T}}{\partial x_b} = \frac{\partial^2 \tilde{T}}{\partial y_b^2}. \tag{3.6}$$

The linearised boundary conditions are given by

$$\tilde{U}(x_b, 0) = 0, \quad \tilde{V}(x_b, 0) = 0, \quad \tilde{T}(x_b, 0) = \tilde{T}_w(x_b), \tag{3.7a-c}$$

$$\tilde{U} \to \mathcal{A}_1(x_b) + \tilde{H}(x_b), \quad \mathcal{K}_1(x_b) = -\int_0^\infty \tilde{T}(x, \eta) \, \mathrm{d}\eta + \mathcal{A}_1(x_b), \tag{3.8a,b}$$

$$\tilde{T}(x_b, \infty) \to 0 \quad \text{as } y_b \to \infty, \tag{3.9}$$

$$\mathcal{A}_1(-\infty) = 0 \quad \text{and} \quad \mathcal{K}_1''(x_b) = -\frac{1}{\pi} \fint_{-\infty}^\infty \frac{\tilde{P}'(s)}{x_b - s} \, \mathrm{d}s. \tag{3.10a,b}$$

We will use Fourier transforms to solve the above equations. The Fourier transform of $g(x_b)$ and the inverse transform are defined by

$$\hat{g}(\omega) = \int_{-\infty}^\infty g(x_b) \mathrm{e}^{-\mathrm{i}\omega x_b} \, \mathrm{d}x_b, \quad g(x_b) = \frac{1}{2\pi} \int_{-\infty}^\infty \hat{g}(\omega) \mathrm{e}^{\mathrm{i}\omega x_b} \, \mathrm{d}\omega. \tag{3.11a,b}$$

After applying the Fourier transformation, the linear equations may be solved to obtain expressions for the perturbed pressure gradient and wall shear distributions as

$$\frac{\partial \tilde{P}}{\partial x_b} = \frac{\mathrm{Ai}'(0)}{2\pi \mathrm{Ai}(0)} \int_{-\infty}^{\infty} \frac{(\mathrm{i}\omega)^{5/3}\hat{f}(\omega) + (\mathrm{i}\omega)^2 \hat{H}(\omega)\Lambda}{\mathrm{isgn}(\omega)\Theta + (\mathrm{i}\omega)^{4/3}} \mathrm{e}^{\mathrm{i}\omega x_b}\, \mathrm{d}\omega \tag{3.12}$$

and

$$\frac{\partial \tilde{U}}{\partial y_b}(x_b, 0) = \frac{1}{2\pi} \int_{-\infty}^{\infty} \frac{(\mathrm{i}\omega)^{4/3}\hat{f}(\omega) + (\mathrm{i}\omega)^{5/3}\hat{H}(\omega)\Lambda}{\mathrm{isgn}(\omega)\Theta + (\mathrm{i}\omega)^{4/3}} \mathrm{e}^{\mathrm{i}\omega x_b}\, \mathrm{d}\omega, \tag{3.13}$$

where $\Theta = -(\mathrm{Ai}'(0)/(\int_0^\infty \mathrm{Ai}(z)\,\mathrm{d}z))$ and $\Lambda = \mathrm{Ai}(0)/(\int_0^\infty \mathrm{Ai}(z)\,\mathrm{d}z)$, and $\hat{f}$ is the transform of the wall temperature $\tilde{T}_w(x_b)$. The multi-valued functions are defined such that we have taken a branch cut along the positive imaginary axis for $\omega$.

The expressions for the pressure and wall shear can be inverted for various wall shapes and heating profiles (see the supplementary material for this paper available at https://doi.org/10.1017/jfm.2017.277). For example, if we assume that the heating region is located in $|x_b| < 0.5$, the wall temperature function is given by

$$\tilde{T}(x_b, 0) = \begin{cases} 0.2, & |x_b| < 0.5, \\ 0, & |x_b| > 0.5 \end{cases} \tag{3.14}$$

and the hump shape is given by

$$\tilde{H}(x_b) = \tilde{h}\exp(-5x_b^2), \tag{3.15}$$

then

$$\hat{f}(\omega) = \frac{0.4}{\omega}\sin\left(\frac{\omega}{2}\right), \quad \mathcal{F}\{\tilde{H}(x_b)\} = \hat{H}(\omega) = \tilde{h}\frac{\sqrt{5\pi}}{5}\exp\left(-\frac{\omega^2}{20}\right). \tag{3.16a,b}$$

A plot of the hump profiles used in the linear and nonlinear computations in comparison to the extent of the heated region can be seen in figure 1. In figure 2(*a,b*), we present the pressure $\tilde{P}(x_b)$ and the wall shear $\tilde{\tau} = (\partial \tilde{U}/\partial y_b)(x_b, 0)$ distributions for different values of the hump height $\tilde{h}$. In figure 2(*a*), we can see that the pressure increases as $x_b$ increases ahead of the hump but drops significantly on reaching the beginning of the heating region at $x_b = -0.5$, followed by recovery at the end of the heated region. The wall shear distribution in figure 2(*b*) decreases initially, but there is a sharp rise and drop on entering and leaving the heated region. The discontinuous changes for $\tilde{h} = 0$ at the start and end of the heated region are also seen in the results of Koroteev & Lipatov (2012). The main difference between the flat-plate case with $\tilde{h} = 0$ and the humped shape is that the presence of the hump creates a larger pressure drop and much larger rise in the wall shear stress across the heated part compared with the flat-plate case. Moreover, the sharp discontinuous change seen in the pressure and the wall shear distribution for the flat-plate case is smoothed out for the hump-shaped profile.

## 4. The nonlinear theory

### 4.1. *Numerical method to solve the nonlinear problem*

The triple-deck equations are nonlinear, and in order to solve them we can use various numerical methods. In Sychev *et al.* (1998), different approaches are described to
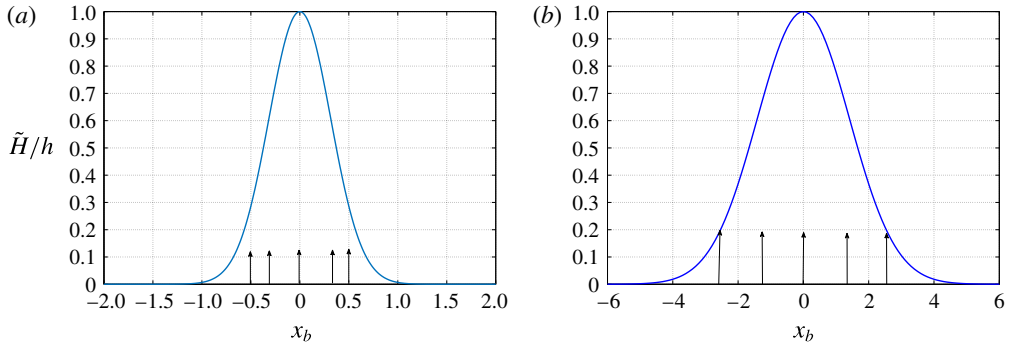
FIGURE 1. Plots of the hump shapes (*a*) $\tilde{H}(x_b)/\tilde{h} = \mathrm{e}^{-5x_b^2}$ and (*b*) $\tilde{H}(x_b)/\tilde{h} = \mathrm{e}^{-0.25x_b^2}$. The arrows depict the extent of the heated region for $|x_b| < a/2$.
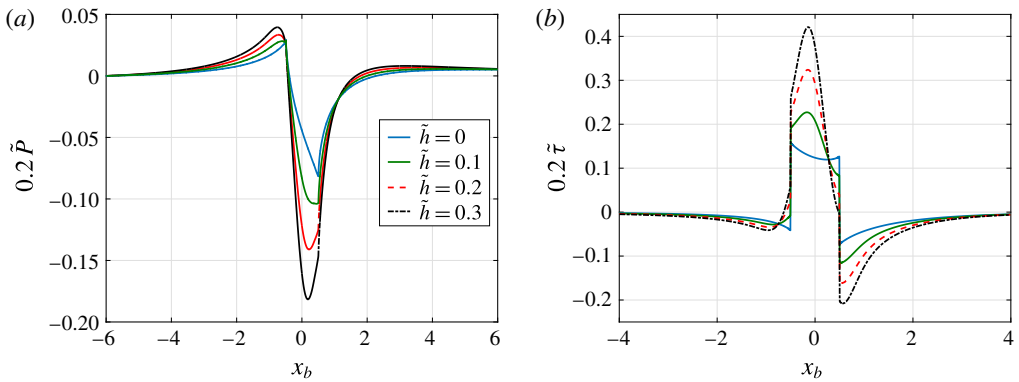


FIGURE 2. Distributions of (*a*) the pressure and (*b*) the wall shear for various values of $\tilde{h}$ in the linear approximation.

solve these kinds of problems. Our method consists of using finite differences in the *x*-direction (streamwise direction) and the Chebyshev collocation method in the *y*-direction (wall normal direction) using the technique as described in Korolev, Gajjar & Ruban (2002) and Logue (2008). Hereafter, the subscript *b* on the variables is omitted. In the *y*-direction, we work with a finite domain $[0, y_{max}]$, where $y_{max}$ is a suitably chosen large value. In the *x*-direction, we have a truncated domain $[x_{min}, x_{max}]$. The *y*-component of the node $(x_i, y_k)$ is given by the Chebyshev collocation points, which are represented using the mapping $y \rightarrow z \subseteq (-1, 1)$ in Chebyshev space so that the collocation points are given by $z = z_j = -\cos(j\pi/N)$, $j = 0, 1, \ldots, N$ and $y = y(z_k) = y_k = (y_{max}(z_k + 1))/2$, $k = 0, 1, \ldots, N$, where $N + 1$ is the number of points in the *y*-direction. Finite differences are used to discretise the *x*-direction. The finite difference points are given by $x = x_i = x_{min} + (i - 1)\Delta x$, $i = 1, 2, \ldots, M$, where $\Delta x = (x_{max} - x_{min})/(M - 1)$.

The interaction law equation can be written as $\partial p/\partial x = -(1/\pi) \int_{-\infty}^{\infty} (\mathcal{K}''(s)/(s - x)) \, \mathrm{d}s$. In order to discretise this, we use the method as presented in Kravtsova, Zametaev & Ruban (2005) to isolate the singular part near $s = x$ and utilise local expansions in the vicinity of the singular point. Finally, using Newton linearisation,

and by defining the unknown variables as

$$\underline{\mathcal{L}}_i = (\underline{U}_i, \underline{T}_i, P_i, \mathcal{A}_i, K_i)^{\mathrm{T}}, \tag{4.1}$$

the linearised discrete equation system can be written as

$$\boldsymbol{A}_i\underline{\mathcal{L}}_{i-2} + \boldsymbol{B}_i\underline{\mathcal{L}}_{i-1} + \boldsymbol{C}_i\underline{\mathcal{L}}_i + \boldsymbol{F}_i\underline{\mathcal{L}}_{i+1} + \boldsymbol{E}_i\underline{\mathcal{L}}_{i+2} = \underline{rhs}_i. \tag{4.2}$$

Here, the block matrices $\boldsymbol{A}_i$, $\boldsymbol{B}_i$, $\boldsymbol{C}_i$, $\boldsymbol{F}_i$ and $\boldsymbol{E}_i$ are of size $(2N+5) \times (2N+5)$. It should be noted that, from the interaction law, the additional terms that do not contribute to the block pentadiagonal structure above are transferred to the right-hand side, treating them as known quantities. This discrete system is applied to $3 \leqslant i \leqslant (M-2)$, while for $i < 3$ we impose values that are given by undisturbed boundary layer profiles, i.e. $U = y, T = 1, K = 0$ and $P = 0$. For $i > (M-2)$, one-sided differences are used. A detailed description of the full discretised equation system can be found in Aljohani (2016). The linear equations are solved directly using a solver that exploits the block pentadiagonal sparsity pattern of the matrices in (4.2).

## 4.2. *Results and discussion*

In this section, we present results from the numerical solution of the nonlinear triple-deck problem for subsonic flow past a MEMS-type heating element. The results depend on the hump shape, which is chosen as

$$H(x_b) = h\mathrm{e}^{-0.25x_b^2}, \tag{4.3}$$

with parameter $h$, and also on the wall temperature, given by

$$T_w(x_b) = \begin{cases} 1 + \Delta T, & |x_b| \leqslant \dfrac{a}{2}, \\ 1, & |x_b| > \dfrac{a}{2}, \end{cases} \tag{4.4}$$

with the parameter $\Delta T$ being the amplitude of perturbations of the temperature and $a$ being the extent of the heated region. It should be noted that for the nonlinear results the hump shape is vanishingly small for $|x_b| > 5$, as can be seen in figure 1.

Koroteev & Lipatov (2012) investigated the problem of a subsonic laminar boundary layer with local heated elements placed along the surface. A comparison of the wall shear distribution obtained in Koroteev & Lipatov (2012) and by the present numerical method is shown in figure 3, with $\Delta T = 0.2$, $h = 0$ and $a = 14$. Excellent agreement between the results can be seen. The results of previous work, here and later, are reproduced using digitising software developed by Rohatgi (2010). Various grid sizes and other checks are carried out to justify that the results are consistent, as detailed in Aljohani (2016).

In the remainder of the results presented below, we have fixed $a = 10$. A comparison of the linear and nonlinear results is shown in figure 4(*a,b*), where we present the normalised pressure and wall shear distributions, with $\Delta T = 0.3$ and $h = 0.2$. It can be seen that, for these values of $h$, the linear approximation is not that different from the nonlinear results. One additional feature that can be noticed in figure 4(*a*) compared with figure 2(*a*) is the rise and dip in pressure on the rear portion of the hump. In figure 2(*a*), the heating was confined to a small part of the hump, whereas in figure 4(*a*), the heating extends to $x_b = 5$, which effectively coincides with the start
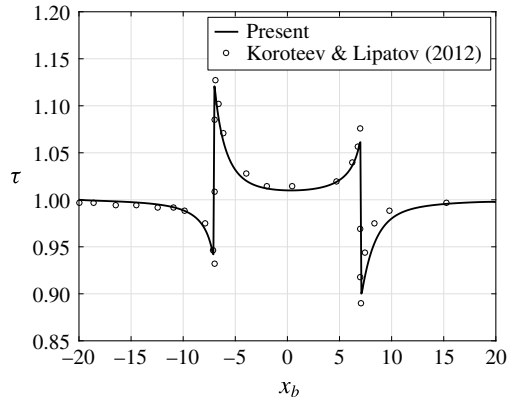
FIGURE 3. A comparison of the present results with those of Koroteev & Lipatov (2012) for the wall shear, with $\Delta T = 0.2$, $a = 14$ and $h = 0$.
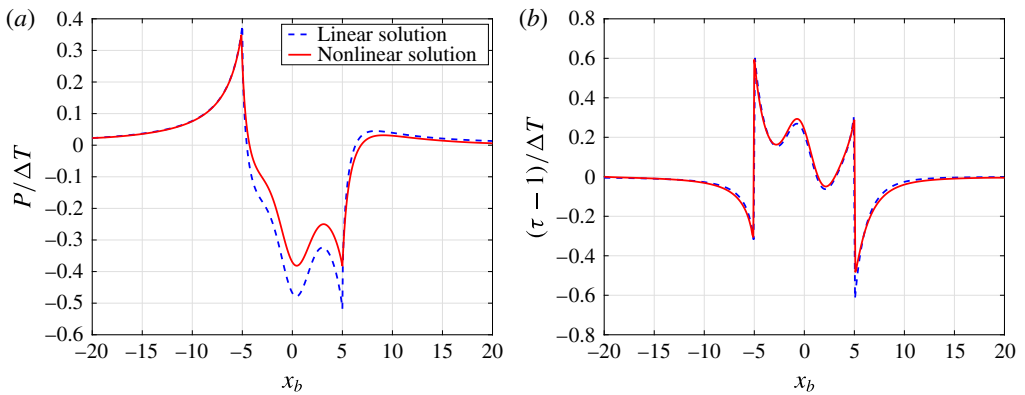


FIGURE 4. Comparisons of the nonlinear and linear results for (*a*) pressure and (*b*) wall shear, with $\Delta T = 0.3$, $a = 10$ and $h = 0.2$.

of the flat-plate region. Once the heating is switched off, the pressure rises rapidly in both cases. In figure 4(*b*), the rise and fall in the pressure over the rear portion of the hump also gives rise to a dip and rise in the wall shear in the same region. In figure 5, we have plotted the maximum and minimum values of the wall shear for a larger value of $h = 0.6$, for varying values of $\Delta T$. Significant differences between the linear and nonlinear results only show up after $\Delta T$ exceeds 1 for the maximum wall shear.

Further nonlinear results are presented in figure 6(*a*,*b*), keeping the hump size fixed with $h = 0.5$ and with the wall temperature varying. It can be observed that increase in $\Delta T$ increases the pressure and wall shear maximum values, which are located on the upstream edge of the heated region, and decreases the pressure and wall shear minimum values, which are located on the downstream edge of the heating region. Once the heating starts, the flow becomes more strongly attached over the hump, although there is still a local rise and fall in the pressure over the rear portion of the hump. Figure 7(*a*,*b*) presents distributions of the pressure and skin friction keeping the heating the same with $\Delta T = 0.4$ while the hump height $h$ varies. It can be noticed that
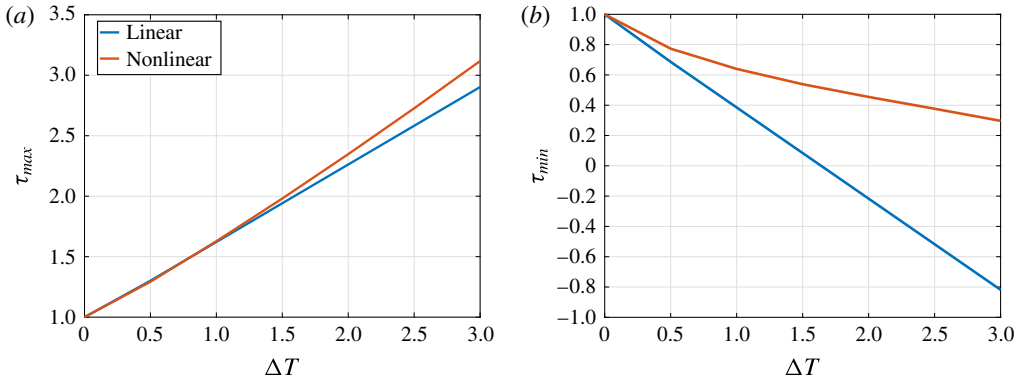
FIGURE 5. Amplitudes of perturbations of the temperature $\Delta T$ versus (*a*) maximum wall shear values and (*b*) minimum wall shear values, with $a = 10$ and $h = 0.6$.
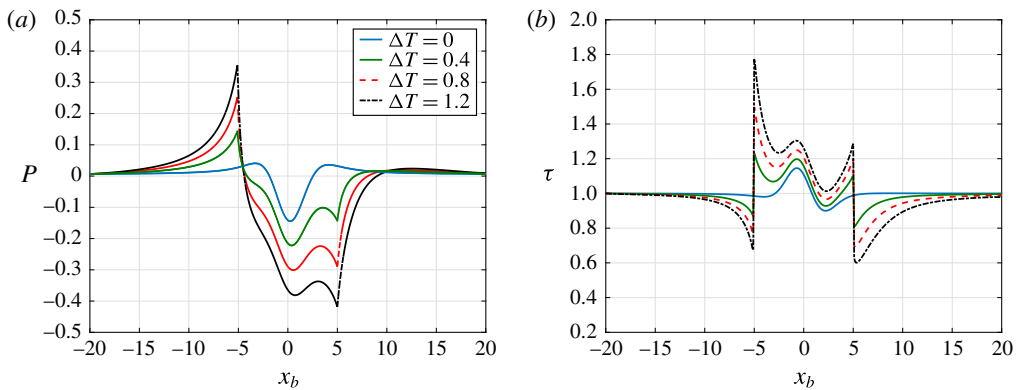


FIGURE 6. (*a*) Pressure and (*b*) wall shear for $h = 0.5$ and various values of $\Delta T$.

increase in $h$ leads to shifts in the maximum and minimum values of the pressure and wall shear to be in the neighbourhood of the centre of the element rather being on its edges. Increase in the hump height also promotes a much stronger adverse pressure gradient on the rear portion of the hump.

## 5. Conclusion

The linear and nonlinear problems of subsonic flow past a heating element have been discussed, and numerical methods were used to solve the linear and nonlinear problems. The results for the heated hump are new and have not been seen before. Our results have been shown to compare well with previous work for the flat-plate case. We have shown that having a shorter hump with heating applied only to the middle part of the hump smooths out the sharp variations in the wall shear and temperature near the start and end of the heated region. Further, a shorter taller hump generally enhances the favourable properties of the heated element in creating a stronger attached flow. Moreover, for longer humps, the presence of the hump creates large peaks and troughs in the pressure and wall shear, particularly near the centre of the hump. These are not observed in the flat-plate case.
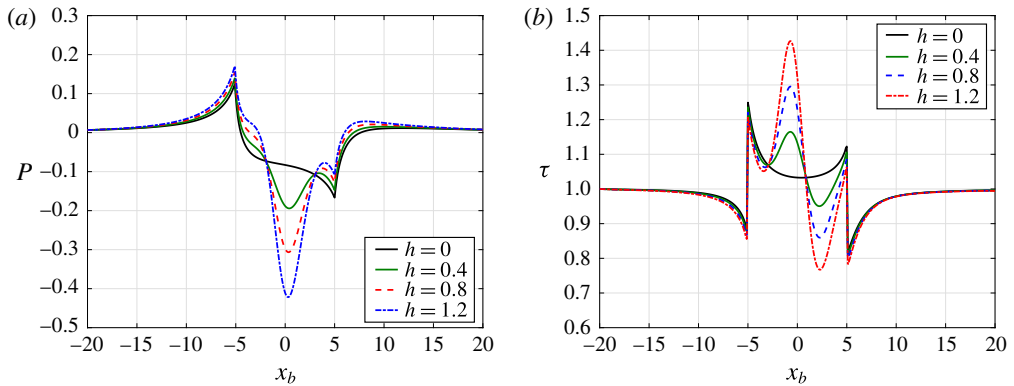
**821** R2-9

FIGURE 7. (*a*) Pressure and (*b*) wall shear for $\Delta T = 0.4$ and various values of $h$.

Clearly, the size and shape of the hump and the location of the heating region are important factors to be taken into consideration in designing suitable MEMS devices that can be used to control the flow and separation.

## Supplementary material

Supplementary material is available at https://doi.org/10.1017/jfm.2017.277.

## References

ALJOHANI, A. F. 2016 Applications of triple deck theory to study the flow over localised heating elements in boundary layers. PhD thesis, University of Manchester.

KOROLEV, G. L., GAJJAR, J. S. B. & RUBAN, A. I. 2002 Once again on the supersonic flow separation near a corner. *J. Fluid Mech.* **463**, 173–199.

KOROTEEV, M. V. & LIPATOV, I. I. 2012 Local temperature perturbations of the boundary layer in the regime of free viscousin–viscid interaction. *J. Fluid Mech.* **707**, 595–605.

KOROTEEV, M. V. & LIPATOV, I. I. 2013 Steady subsonic boundary layer in domains of local surface heating. *Z. Angew. Math. Mech.* **77**, 486–493.

KRAVTSOVA, M. A., ZAMETAEV, V. B. & RUBAN, A. I. 2005 An effective numerical method for solving viscous–inviscid interaction problems. *Phil. Trans. R. Soc. Lond.* **363**, 1157–1167.

LIPATOV, I. I. 2006 Disturbed boundary layer flow with local time-dependent surface heating. *Fluid Dyn.* **41**, 55–65.

LOGUE, R. P. 2008 Stability and bifurcations governed by the triple-deck and related equations. PhD thesis, University of Manchester.

MESSITER, A. F. 1970 Boundary-layer flow near the trailing edge of a flat plate. *SIAM J. Appl. Maths* **18**, 241–257.

NEILAND, V. Y. 1969 Theory of laminar boundary layer separation in supersonic flow. *Izv. Akad. Nauk SSSR Mekh. Zhidk. Gaza* **4**, 53–57.

NEILAND, V. Y. 1971 The asymptotic theory of the interaction of a supersonic flow with a boundary layer. *Izv. Akad. Nauk SSSR Mekh. Zhidk. Gaza* **4**, 41–47.

ROHATGI, A. 2010 Webplotdigitizer. http://arohatgi.info/WebPlotDigitizer.

SMITH, F. T. 1973 Laminar flow past a small hump on a plate. *J. Fluid Mech.* **57**, 803–824.

STEWARTSON, K. & WILLIAMS, P. G. 1969 Self-induced separation. *Proc. R. Soc. Lond.* A **312**, 181–206.

SYCHEV, V. V., RUBAN, A. I., SYCHEV, V. V. & KOROLEV, G. L. 1998 *Asymptotic Theory of Separated Flows*. Cambridge University Press.